JACS
JOURNAL OF THE AMERICAN CHEMICAL SOCIETY

Article

pubs.acs.org/JACS

Engineering the Edges of MoS_2 (WS_2) Crystals for Direct Exfoliation into Monolayers in Polar Micromolecular Solvents

Xiao Hai,[†,‡,⊥] Kun Chang,[*,‡,⊥] Hong Pang,[†,‡] Mu Li,[†,‡] Peng Li,[‡] Huimin Liu,[‡] Li Shi,[†,‡] and Jinhua Ye[*,†,‡,#,§]

[†]Graduate School of Chemical Science and Engineering, Hokkaido University, Sapporo 060-0814, Japan

[‡]Photocatalytic Materials Group, International Center for Materials Nanoarchitectonics (WPI-MANA), National Institute for Materials Science, 1-1 Namiki, Tsukuba, Ibaraki 305-0044, Japan

[#]TU-NIMS Joint Research Center, School of Materials Science and Engineering, Tianjin University, 92 Weijin road, Tianjin 300072, P. R. China

[§]Collaborative Innovation Center of Chemical Science and Engineering (Tianjin), Tianjin 300072, P. R. China

Supporting Information

ABSTRACT: Synthesizing transition metal dichalcogenide (TMDC) monolayers through the liquid exfoliation of bulk crystals in low boiling point polar micromolecular solvents, such as water, is paramount for their practical application. However, the resulting hydrodynamic forces only appear on the crystal edges due to the mismatch in surface tension between the polar micromolecular solvents and the bulk crystals and are insufficient to overcome the strong van der Waals attraction between adjacent microscale layers. Herein, we present the novel strategy of engineering the lateral size of TMDC (MoS_2 and WS_2) crystals in the nanoscale to increase the fraction of edges, leading to their direct and ready exfoliation in polar micromolecular solvents, even in pure water, to produce monolayer MoS_2 and WS_2 nanosheets in high yield. To examine one of their important applications, their catalytic hydrogen evolution activities were evaluated when used as cocatalysts with a photoharvester semiconductor (cadmium sulfide, CdS) in a reaction driven by solar energy. These exfoliated MoS_2 (WS_2) monolayers exhibited superior cocatalytic performance in the photocatalytic hydrogen evolution reaction (HER). Notably, the cocatalytic performance of monolayer WS_2 nanosheets is even higher than that of platinum (Pt), which is a state-of-the-art catalyst for catalytic hydrogen evolution. This work elucidates the importance of decreasing the lateral size of layered crystals to significantly enhance their exfoliability, providing a new strategy for the large-scale preparation of nanoscale TMDC monolayers by liquid exfoliation.

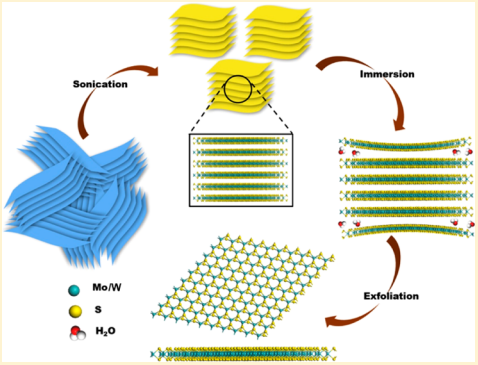

INTRODUCTION

Pioneering works have shown that monolayer transition metal dichalcogenides (TMDCs) bear great promise as two-dimensional materials because of their intrinsic semiconducting characteristics compared with the gapless nature of graphene.[1−5] Among them, monolayer molybdenum disulfide (MoS_2) and tungsten disulfide (WS_2) are notable due to having direct bandgaps, large in-plane electron mobilities (>200 cm^{-2} V^{-1} s^{-1}), high current on/off ratios, remarkable mechanical and optical properties, and high catalytic activity in the hydrogen evolution reaction (HER).[6−11] In general, large lateral size, high crystallinity, and defect-free morphologies are required in physical applications such as transistors, photodetectors, and electroluminescent devices.[5,12,13] Alternatively, in the catalysis of HER, possessing large specific surface areas and a larger number of exposed active sites are beneficial.[14,15] Density function theory (DFT) calculation and corresponding experiments have revealed that the activity of MoS_2 (WS_2) in HER can be attributed to the edge-site S atoms, which have a free energy of hydrogen adsorption (ΔG_H^*) close to zero when catalyzing H_2 evolution.[14,16] Despite the fact that monolayer MoS_2 and WS_2 can be good candidates for HER owing to their relatively low cost, natural abundance, high catalytic activity, and good stability, large-scale production of monolayer MoS_2 and WS_2 is still a challenge.[17,18]

Over the past years, tremendous effort has been made toward the reliable and scaled-up production of atomically thin TMDC nanosheets.[13] Among the methods, liquid phase exfoliation, first utilized by Coleman and colleagues, is considered to be the most promising route toward the large-scale production of monolayer and few-layer MoS_2 (WS_2).[19−22] Currently, there are two major issues restricting further application and development of this method. First and foremost is the low yield in monolayer production, where most of the products are few-layer nanosheets.[13,23] Second, this method is highly

Received: August 4, 2016
Published: October 27, 2016

DOI: 10.1021/jacs.6b08096
J. Am. Chem. Soc. 2016, 138, 14962−14969

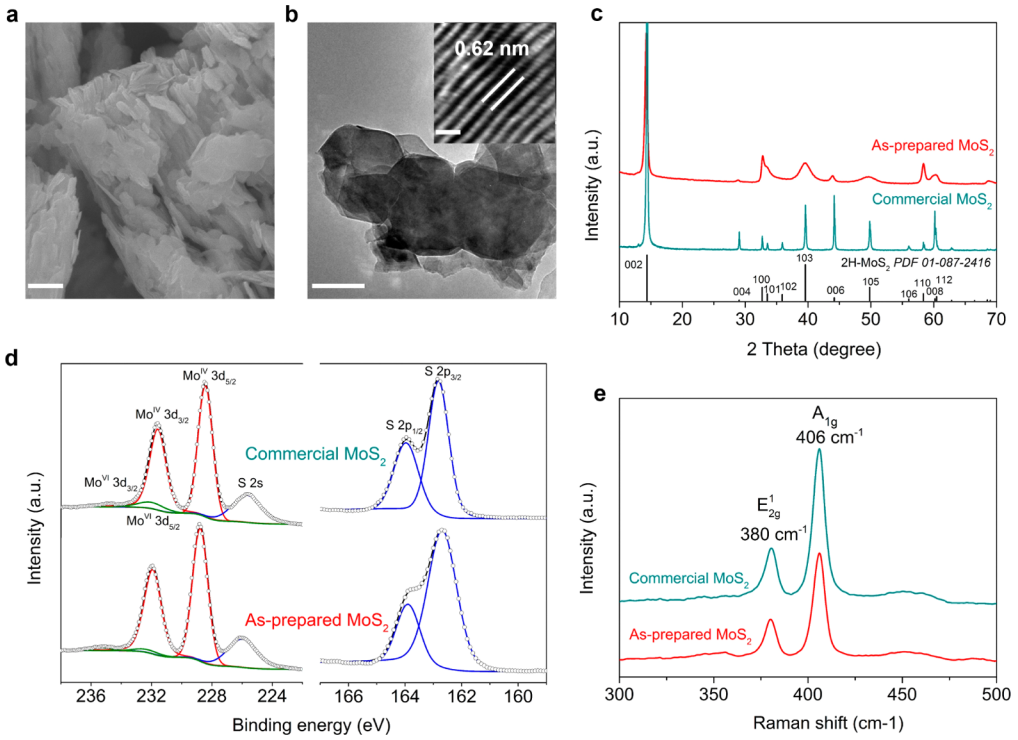

Figure 1. (a) SEM image of the as-prepared MoS_2 crystals. Scale bar = 200 nm. (b) TEM image of the as-prepared MoS_2 crystals. Scale bar = 100 nm. Inset is the high-resolution TEM image. Scale bar = 1 nm. (c) XRD patterns of the as-prepared and commercial MoS_2. The standard diffraction peak position of 2H-MoS_2 is displayed at the bottom of the diagram. (d) Fitted XPS Mo 3d, S 2s, and S 2p core-level spectra of the as-prepared and commercial MoS_2. (e) Raman spectra of the as-prepared and commercial MoS_2.

dependent on the solvent. Thus, far, *N*-methyl-2-pyrrolidone and other pyrrolidone-based solvents have been found to be the most compatible solvents for MoS_2 (WS_2) exfoliation.[20] Generally, pyrrolidone-based solvents can sufficiently intercalate into the inner layers of the crystals due to the compatible surface tension between the liquid solvents and the bulk MoS_2 (WS_2) crystals. Then, the generated cavitation bubbles inside of the crystals can delaminate the layered crystallites to produce exfoliated ultrathin nanosheets. However, these pyrrolidone-based solvents are generally toxic and have high-boiling points, which poses a significant environmental risk at the industrial scale. Even though many attempts have been made to exfoliate bulk MoS_2 (WS_2) crystals in low boiling point polar micromolecular solvents, such as water, via probing surface tension components or through temperature control, neither the concentration of dispersions nor the monolayer yield were satisfactory.[23,24] Owing to the mismatch in surface tension between polar micromolecular solvents (water, ethanol, and methanol) and bulk crystals, hydrodynamic force from the collapse of cavitation bubbles can only appear on the crystal edges, which is insufficient to overcome the strong van der Waals attraction between microscale adjacent layers of commercial MoS_2 (WS_2).[23] Overcoming these disadvantages and achieving the highly efficient exfoliation of bulk MoS_2 (WS_2) crystals into monolayers in low boiling point polar micromolecular solvents, such as water and ethanol, is a challenge and of great interest.

In this paper, inspired by the unique layered structural properties of MoS_2 (WS_2), we tailor their lateral size to the nanoscale to increase the fraction of edges. As expected, the obtained MoS_2 (WS_2) crystals can be efficiently exfoliated to monolayer MoS_2 (WS_2) nanosheets in low boiling point polar micromolecular solvents, even in pure water, without the use of any surfactant. Our strategy for preparing MoS_2 (WS_2) monolayers improves not only the monolayer yield but also the stability of the monolayer nanosheets in polar micromolecular solvents with low boiling points, making them highly useful.

RESULTS AND DISCUSSION

The morphologies, structure, and chemical states of the as-prepared MoS_2 (WS_2) precursors were examined by scanning electron microscopy (SEM), transmission electron microscopy (TEM), X-ray diffraction (XRD), X-ray photoelectron spectroscopy (XPS), and Raman spectroscopy. Compared with commercial MoS_2 (Figure S1), the lateral size of the as-prepared MoS_2 precursor was drastically decreased from the microscale to the nanoscale, as shown in the SEM (Figure 1a) and TEM (Figure 1b) images. An estimation of the lateral size from the full-width at half-maximum of the (110) reflection in the XRD pattern (Figure 1c) is approximately 160 nm. Furthermore, the (002) peak is characterized by a shift to a lower angle compared with commercial MoS_2 and the 2H-MoS_2 crystal (PDF 01-087-2416). This shift in the (002) peak indicates an enlarged interlayer distance of the as-prepared MoS_2 precursor.[25,26] According to the Bragg equation, the interlayer distance is calculated to be 0.62 nm, which is in agreement with the observed result in high-resolution TEM (inset of Figure 1b and Figure S2). It is worth noting that despite the significantly decreased lateral size, the as-prepared MoS_2 precursor still maintains high crystallinity, as shown by the sharp (002) peak observed in the XRD pattern and the uniform lattice arrangement in the high-resolution TEM image.

DOI: 10.1021/jacs.6b08096
J. Am. Chem. Soc. 2016, 138, 14962−14969

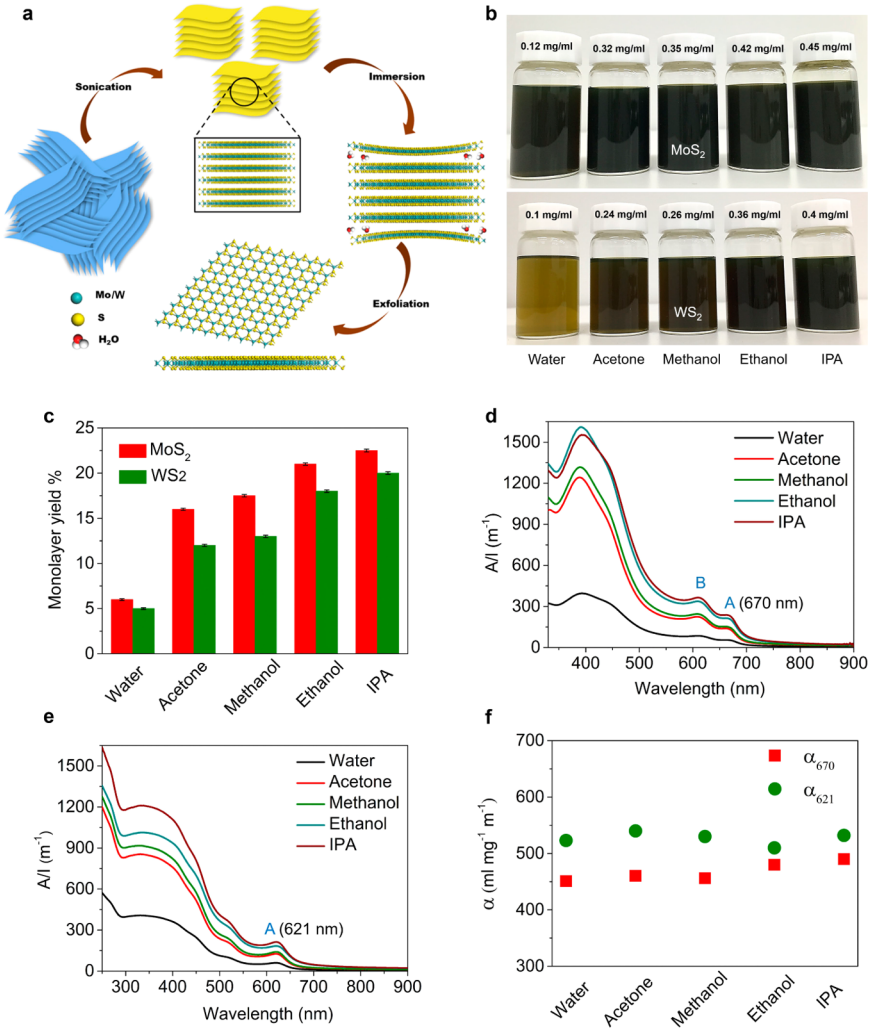

Figure 2. (a) Proposed mechanism of the liquid exfoliation process. (b) Photographs of obtained MoS_2 and WS_2 dispersions. (c) Monolayer yield. (d) Absorption spectra of MoS_2 dispersions. The positions of A- and B-excitons are marked. (e) Absorption spectra of WS_2 dispersions. The position of the A-exciton is marked. (f) Absorption coefficients at the A-exciton.

The chemical states of Mo and S in the as-prepared MoS_2 precursor were investigated by XPS (Figure 1c). The Mo 3d, S 2s, and S 2p spectra of the as-prepared MoS_2 precursor are similar to those of commercial MoS_2. According to the analysis of the Mo 3d spectra, most of the Mo signals arise from the $3d_{3/2}$ peak at 232.0 eV and the $3d_{5/2}$ peak at 229.2 eV, indicating the characteristic +4 oxidation state.[15] For both as-prepared and commercial MoS_2, deconvolution of the Mo 3d peaks revealed a weak Mo^{6+} 3d doublet with the $3d_{5/2}$ peak at 232.5 eV and $3d_{3/2}$ peak at 235.5 eV, likely due to slight surface oxidation upon exposure to air. In the S 2p core-level spectra, only a single doublet was observed at 163.6 and 162.5 eV corresponding to S $2p_{1/2}$ and S $2p_{3/2}$ orbitals of divalent sulfide ions, which is in good agreement with the binding energy of S^{2-} ions in 2H-MoS_2.[27] Raman spectroscopy, shown in Figure 1d, further confirmed the 2H-phase structure of the as-prepared MoS_2 precursor by the appearance of two distinct peaks at 380 and 406 cm^{-1}, which correspond to the in-plane vibration (E_{2g}^1) and out-of-plane mode (A_{1g}), respectively.[28] These results indicate that highly pure and highly crystalline 2H-phase MoS_2 crystals with lateral sizes in the nanoscale can be successfully synthesized through the facile thermal decomposition of $(NH_4)_2MoS_4$. Furthermore, the 2H-phase of WS_2 crystals can also be successfully synthesized (Figure S3).

In an ideal liquid exfoliation, sufficient liquid intercalation into the layered crystal is the most effective and straightforward method to reduce the strength of the interlayer van der Waals attractions.[29] Upon interaction with ultrasonic waves, the generated cavitation bubbles inside of the crystals collapse into high-energy liquid jets, breaking up the layered crystallites and producing exfoliated ultrathin nanosheets.[23] However, the mismatch in surface tension between common polar micromolecular solvents, such as water, and MoS_2 (WS_2) crystals will hamper the intercalation of solvent into the layered crystals.[20] High-energy liquid jets can only be generated at the interlayer edges rather than in the inner layers. For commercial MoS_2 and WS_2 crystals with lateral dimensions in the microscale, the resulting hydrodynamic forces around the crystal edge are insufficient to overcome the strong van der Waals attraction between the large adjacent layers, making direct exfoliation difficult. When the lateral size of the MoS_2 (WS_2) crystals is reduced from the microscale to the nanoscale, the ratio of hydrodynamic forces to interlayer van der Waals forces will be improved. Thus, for as-prepared MoS_2 and WS_2 crystals with lateral sizes on the nanoscale, the resulting hydrodynamic

DOI: 10.1021/jacs.6b08096
J. Am. Chem. Soc. 2016, 138, 14962−14969

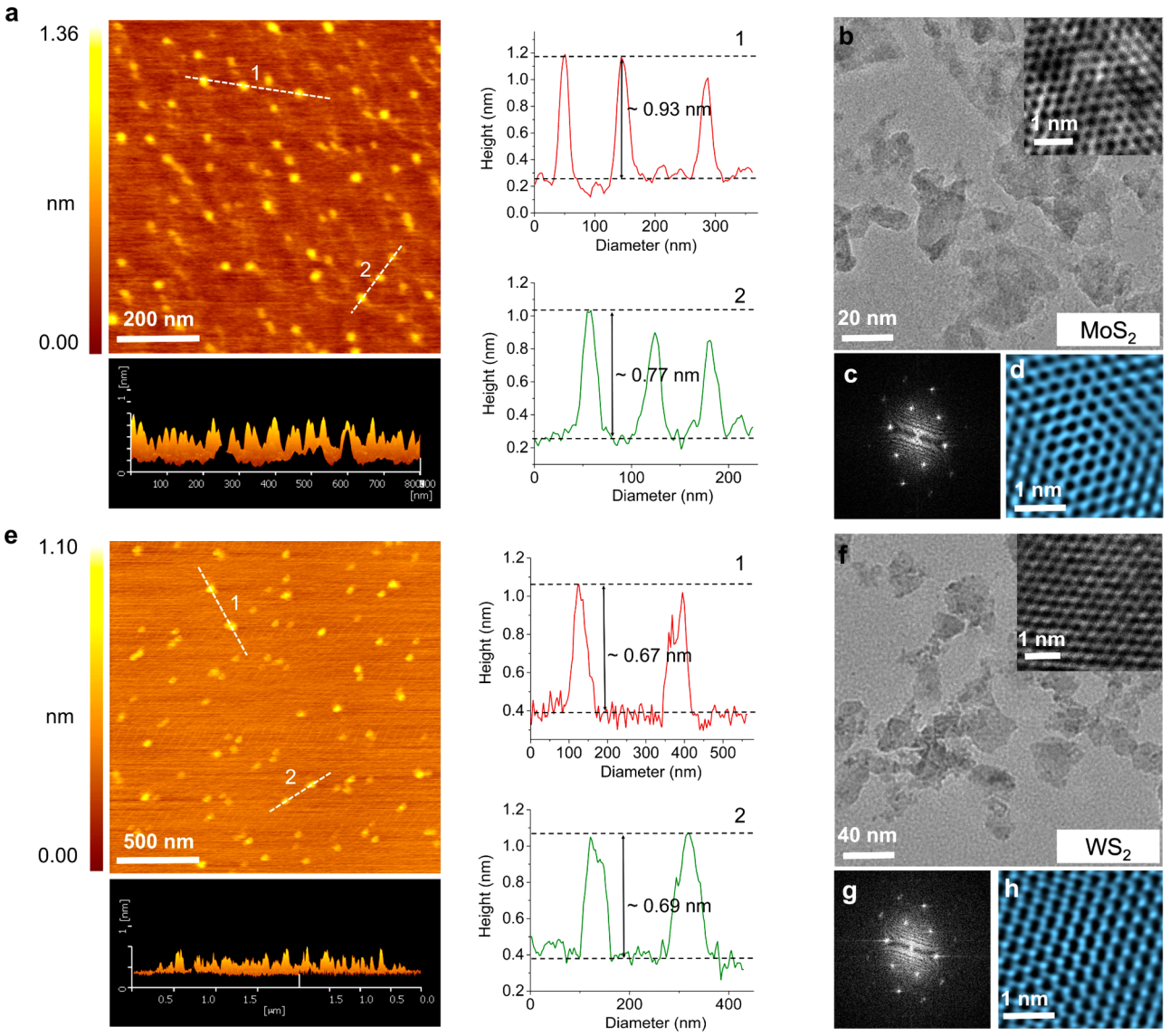

Figure 3. (a) AFM image, 3D AFM image (bottom), and height profile of exfoliated monolayer MoS_2 nanosheets. (b) TEM image of monolayer MoS_2 nanosheets. Inset is the high-resolution TEM image of the selected region. (c, d) FFT pattern and FFT-filtered atomic resolution image of MoS_2. (e) AFM image, 3D AFM image (bottom), and height profile of exfoliated monolayer WS_2 nanosheets. (j) TEM image of monolayer WS_2 nanosheets. Inset is the high-resolution TEM image of the selected region. (g, h) FFT pattern and FFT-filtered atomic resolution image of WS_2.

forces from high-energy liquid jets at the edge sites are enough to overcome the interlayer van der Waals attraction, allowing for ready exfoliation in polar micromolecular solvents, even in pure water, without the use of any surfactant. Herein, the following process is proposed for the successful exfoliation of the as-prepared MoS_2 and WS_2 precursors for producing monolayer nanosheets (Figure 2a). Upon sonication, the nanoflakes composed of MoS_2 and WS_2 precursors are first decomposed into individual nanoflakes (Figure S4). Next, the surrounding polar micromolecular solvents intercalate into the edges of the crystal interlayers. Then, the generated high-energy jets around the crystal edges overcome the interlayer van der Waals attraction, leading to the exfoliation and shearing of nanoflakes into monolayer nanosheets. After exfoliation, the exfoliated monolayer nanosheets can stably disperse in the polar micromolecular solvent.

To obtain purely monolayer, the sonicated suspensions of bulk MoS_2 or WS_2 were first centrifuged at 2000 rpm (RCF 760*g*) for 1 h then at 4000 rpm (RCF 3020*g*) for another 1 h to remove nonexfoliated precipitate. Figure 2b shows photographs of the obtained pure monolayer MoS_2 and WS_2 nanosheets in different polar micromolecular solvents, which were stable for over 100 days. Optimization of the exfoliation and dispersion procedure (Figure S5) gave monolayer concentrations as high as 0.12 mg/mL (in water), 0.32 mg/mL (in acetone), 0.35 mg/mL (in methanol), 0.42 mg/mL (in ethanol), and 0.45 mg/mL (in IPA) for MoS_2 and as high as 0.10 mg/mL (in water), 0.24 mg/mL (in acetone), 0.26 mg/mL (in methanol), 0.36 mg/mL (in ethanol), and 0.40 mg/mL (in IPA) for WS_2. The initial concentration of the bulk crystal was 2 mg/mL, and the corresponding monolayer yield (Figure 2c) was calculated to be as high as 21% for MoS_2 and 18% for WS_2 in ethanol. Even in pure water, a monolayer yield of 6% for MoS_2 and 5% for WS_2 can be achieved. It is worth noting that the dispersions were obtained by high-speed centrifugation over long periods of time, which inevitably results in many exfoliated monolayer nanosheets reaggregating or adsorbing on the large sediments and being removed from the suspension.

DOI: 10.1021/jacs.6b08096
J. Am. Chem. Soc. 2016, 138, 14962−14969

Optical absorption spectra (Figure 2d) of the resulting dispersions show features expected for 2H-MoS_2.[30] The distinct two peaks located at 615 (B-exciton) and 670 nm (A-exciton) are assigned to the direct excitonic transitions of MoS_2 at the K point of the Brillouin zone.[31,32] We determined the position of the A-exciton and B-exciton using the second derivative of the absorption spectra to exclude the contribution from the size-dependent scattering background (Figure S6).[33] To simplify the tedious weighting process for determining nanosheet concentration, the concentration can be simply estimated using the optical absorption spectrum and the Beer−Lambert law, which relates the measured absorbance at a given wavelength to the concentration of the dispersion by the formula $A/l = \alpha C$, where A is the absorbance, l is the optical path length, α is the absorption coefficient, and C is the concentration.[20] A/l scaled linearly with C (Figure S7) for all the dispersions, allowing for the calculation of α values. The obtained absorption coefficients of monolayer MoS_2 nanosheets range from 450 to 490 mL mg^{-1} m^{-1} (Figure 2f), which are much smaller than those previously published (~3000 mL mg^{-1} m^{-1}).[20,23] This small α value may be attributed to the higher monolayer ratio and smaller lateral size. Figure 2e shows the optical absorption spectra of WS_2 dispersions exfoliated in different polar micromolecular solvents. A/l also scaled linearly with C (Figure S8). The obtained absorption coefficients of monolayer WS_2 nanosheets were calculated in the range of 510 to 532 mL mg^{-1} m^{-1} (Figure 2f), which are also much smaller than those previously published (~2500 mL mg^{-1} m^{-1}).[20,23]

The thickness of the exfoliated nanosheets was investigated by atomic force microscopy (AFM). We deposited dispersions on mica substrates by pipet and let them dry naturally. The high fluidity and volatility of these solvents allow the dispersed nanosheets to quickly and uniformly deposit on the mica substrates (Figure S9). The height profile of the two selected regions in the AFM images shows a height of ~0.8 nm (±0.2 nm) for MoS_2 (Figure 3a and Figure S10) and ~0.7 nm (±0.1 nm) for WS_2 (Figure 3e and Figure S11), which are close to the theoretical thickness of monolayer MoS_2 and WS_2 (~0.65 nm).[34] This discrepancy is caused by surface corrugation due to distortions. The corresponding 3D images show that the dispersed nanosheets are all thinner than 1 nm, indicating that all the dispersed nanosheets have monolayer structures. To examine another typical characteristic for monolayer MoS_2 and WS_2, their photoluminescence (PL) spectra were also investigated to compare with bulk and partial monolayer dispersions (Figure S12). In agreement with other reports,[21,33] the PL intensity of the A-exciton of the entirely monolayer MoS_2 (WS_2) dispersions was much stronger than their corresponding bulk and partial monolayer dispersions with the same concentration (Figure S13). Low-resolution TEM images (Figure 2b,f) indicate that the lateral size of the MoS_2 and WS_2 monolayers is approximately 40 nm. To further accurately measure the average sheet size, we employed particle size distribution analysis, as shown in Figure S14. The average lateral size was measured to be 46.5 nm for MoS_2 and 48.2 nm for WS_2, which are in good accordance with the results determined by the TEM images. The high-resolution TEM image of MoS_2 (inset of Figure 2b) and WS_2 (inset of Figure 2f) and associated Fourier transforms (Figure 2c,g) from the center of the nanosheets illustrate the hexagonally symmetric structure. The hexagon widths of 3.8 Å for MoS_2 (Figure 3d) and 4.0 Å for WS_2 (Figure 3h) were determined after performing fast Fourier transform filtering of the high-resolution TEM images. These results indicate that the crystal structures obtained for the monolayer MoS_2 and WS_2 nanosheets were not damaged during water-bath sonication and retained their single crystalline nature.[35,36]

Generally, the exfoliated monolayer MoS_2 and WS_2 nanosheets are easily aggregated and restacked due to the weak van der Waals force. It is important to examine the stability of the dispersions after centrifugation. Optical absorption spectra of MoS_2 (Figure 4a) and WS_2 (Figure 4b) dispersions in ethanol

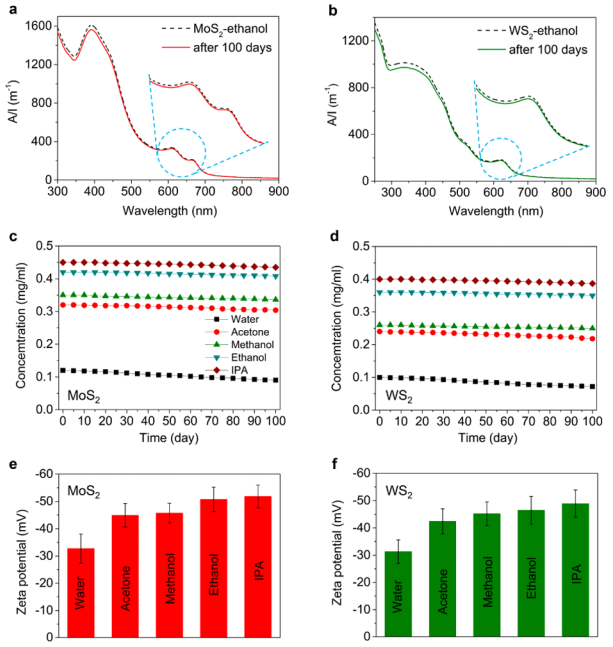

Figure 4. (a, b) Absorption spectra of MoS_2 and WS_2 monolayers dispersed in ethanol before and after storage for 100 days. (c, d) Concentration retention of MoS_2 and WS_2 as a function of time. (e, f) ζ-Potential of MoS_2 and WS_2 dispersions.

indicate that there is little attenuation after 100 days, suggesting the high stability of the monolayer dispersions in ethanol. The dispersion stability was tested by monitoring the change in the optical absorption spectra as a function of time (Figure S15). Concentration retention versus time can be easily calculated from changes in the optical absorption spectra. These data are shown for MoS_2 (Figure 4a) and WS_2 (Figure 4b) dispersions. We found that all of the MoS_2 and WS_2 dispersions, except those in water, are extremely stable, with more than 90% concentration retention after 100 days. Monolayer MoS_2 and WS_2 nanosheets dispersed in water are less stable, with 75% concentration retention for MoS_2 and 72% concentration retention for WS_2. The stability can also be reflected by performing ζ-potential tests, because nanomaterial solution stability is closely related to electrical double layers on the nanomaterial surface.[37] In general, dispersed nanomaterials are stable with ζ-potential values of less than −30 mV.[38,39] Each dispersion was tested three times, and the average value is reported (Figure S16). The measured ζ-potential values of the MoS_2 (Figure 4c) and WS_2 dispersions (Figure 4d) are all less than −30 mV, suggesting that their good stability is irrespective of the solvent. Moreover, the exfoliated monolayer MoS_2 and WS_2 nanosheets are extremely stable when dispersed in acetone, methanol, ethanol, and IPA, with ζ-potential values of less than −40 mV.

DOI: 10.1021/jacs.6b08096
J. Am. Chem. Soc. 2016, 138, 14962−14969

As MoS_2 (WS_2) nanosheets are reported as potential electrocatalysts and cocatalysts to replace Pt in HER,[40−42] we evaluated their HER performance by loading them on commercial CdS to be used as cocatalysts for photocatalytic hydrogen evolution. These monolayer MoS_2 and WS_2 nanosheets can be easily and uniformly adsorbed on the surface of CdS due to their soft and small size features. Considering that the ΔG_H^* of MoS_2 (WS_2) active sites is slightly more than zero,[14] the rate-determining step in HER is the adsorption step. Although an acidic environment with an appropriate amount of H^+ favors HER performance, the photoharvester CdS is not stable in a strongly acidic environment. Thus, the effect of pH value on the photocatalytic H_2 activity of the MoS_2/CdS composite was investigated (Figure S17).

A series of MoS_2/CdS and WS_2/CdS composites with different amounts of cocatalyst were examined to investigate the effect of cocatalyst loading on the photocatalytic H_2 activity (Figure 5a). All of the composites were annealed in an Ar atmosphere at 400 °C for 4 h before testing.[11] It was found that the composites show the highest H_2 evolution activities of 4.28 mmol h^{-1} for MoS_2/CdS with 2 wt % cocatalyst and 5.5 mmol h^{-1} for WS_2/CdS with 3 wt % cocatalyst (Figure S18). Irradiated light will be blocked by the excess of MoS_2 (WS_2) monolayers upon further increasing the amount of cocatalyst, leading to a decrease in the H_2 evolution activity. The higher cocatalytic performance of WS_2 may be related to its stronger metallic properties.[17] In addition to their remarkable photocatalytic activities, these materials also exhibit high stability, and no noticeable loss of activity for photocatalytic H_2 production can be observed after five cycles (Figure 5b). The wavelength dependence of H_2 evolution was then further investigated to prove that the reaction was driven by incident light. The UV−vis absorption spectrum of the CdS photoharvester along with the apparent quantum efficiency (AQE) of MoS_2/CdS and WS_2/CdS composites as a function of incident light wavelength is shown in Figure 5c. The AQE decreased as the wavelength of the monochromatic light increased, which was found to coincide well with the absorption edge of the CdS semiconductor. Under visible light irradiation at 420 nm, the AQE was calculated to be as high as 57.2% for MoS_2/CdS and 71.3% for WS_2/CdS. Figure 4d displays the H_2 production activities of MoS_2/CdS and WS_2/CdS composites under simulated sunlight using an Air Mass (AM) 1.5 solar simulator with a light intensity of 100 mW cm^{-2}. It can be seen that even under an irradiation of AM 1.5, the average hydrogen production of the WS_2/CdS composite can reach ∼500.0 μmol h^{-1}, which is higher than that of MoS_2/CdS (∼397.2 μmol h^{-1}).

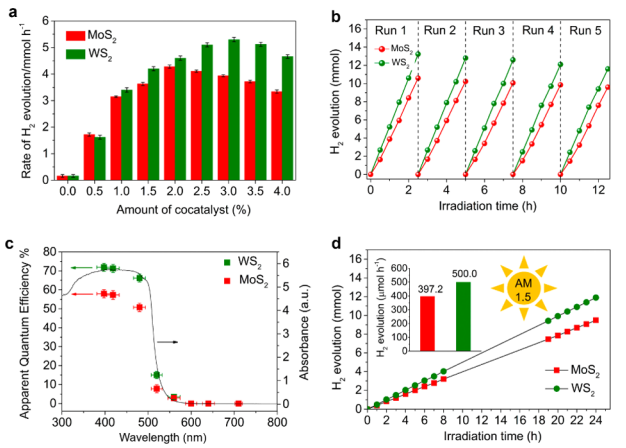

Figure 5. (a) Optimized content of cocatalysts over CdS. (b) Cycling test and (c) wavelength-dependent apparent quantum efficiency of H_2 evolution from MoS_2/CdS with 2 wt % cocatalyst and WS_2/CdS with 3 wt % cocatalyst. Light source: 300-W Xe lamp with a L42 cutoff, λ > 420 nm. Reaction solution: 300 mL of sodium lactate solution (30 vol % lactic acid adjusted by NaOH, pH ≈ 5.0). Catalyst: 200 mg. (d) Photocatalytic H_2 production activities of MoS_2/CdS and WS_2/CdS under the irradiation of AM 1.5 with a light intensity of 100 mW cm^{-2}. The inset shows the average rate of H_2 evolution.

During the photocatalytic HER process, the facile recombination of photoexcited electron−hole pairs before migrating to the surface to take part in the chemical reaction severely restricted the photoconversion efficiency.[43] Noble metals are often selected as cocatalysts to load on the surface of semiconductors to enhance the separation of photoexcited electrons and holes.[17] Pt possesses the highest ability for trapping electrons because of its lowest Fermi level, giving it optimal cocatalytic performance in photocatalytic H_2 evolution.[44] In this work, we compared the cocatalytic performance of the exfoliated monolayer MoS_2 and WS_2 nanosheets with that of Pt (Figure S19). It was found that the H_2 evolution activity of the MoS_2/CdS (4.28 mmol h^{-1}) composite is close to that of Pt/CdS (4.6 mmol h^{-1}), and the monolayer WS_2 (5.5 mmol h^{-1}) nanosheets exhibit an unexpectedly higher cocatalytic performance than Pt. The superior cocatalytic performances of the MoS_2 and WS_2 monolayers are attributed to the following two aspects. First, the monolayer MoS_2 and WS_2 nanosheets with lateral sizes in the tens of nanometers have more active edge sites for HER.[45] The DFT-calculated free energy of atomic hydrogen bonding to MoS_2 edge sites is slightly positive at +0.08 eV.[16] Chorkendorff and co-workers also experimentally determined that the active sites for HER are the MoS_2 edge-site S atoms.[14] Compared with MoS_2 and WS_2 monolayers obtained from commercial bulk crystals (average lateral size >200 nm), our exfoliated monolayer nanosheets (average lateral size <50 nm) have a higher fraction of edges, which provides more exposed active sites for HER. Because of the strong dependence on the layers, the cocatalytic performance of the MoS_2 nanosheets increased with reducing layer number, where monolayer MoS_2 showed the best cocatalytic performance for photocatalytic hydrogen production.[11] The obtained monolayer MoS_2 and WS_2 nanosheets can be uniformly adsorbed on CdS surfaces to avoid aggregation, as seen in the SEM images (Figure S20) and optical absorption spectra of the composites (Figure S21). Second, chemical bonding at the interface of the monolayer nanosheets with CdS is more favorable for interfacial charge transfer, which can efficiently suppress the recombination of photoexcited electron−hole pairs.[46−48] The photocatalytic H_2 activities of MoS_2/CdS and WS_2/CdS composites with different annealing temperatures are shown in Figure S22. It can be seen that the activity gradually increased with increasing temperature and reached a plateau at 400 °C. For the freshly made, mechanically mixed composites, their weak physical adsorption severely lowered their photocatalytic HER activities, and the composites were great strengthened after annealing at 400 °C through the creation of chemical bond. This result indicates that the chemically bonded interface of WS_2/CdS plays an important role in separating photoexcited electron−hole pairs, leading to a higher cocatalytic performance than Pt.

DOI: 10.1021/jacs.6b08096
J. Am. Chem. Soc. 2016, 138, 14962−14969

CONCLUSION

In summary, we have introduced a facile method to synthesize highly crystalline bulk MoS_2 (WS_2) precursors with a lateral size in the nanoscale, which can be readily exfoliated in polar micromolecular solvents, even in pure water, to produce MoS_2 (WS_2) monolayers without the use of any surfactant. Compared to commercial MoS_2 (WS_2), the successful exfoliation of the as-prepared MoS_2 (WS_2) crystals is attributed to their increased fraction of edges, which can improve the ratio of hydrodynamic forces on the edges to van der Waals forces between the adjacent layers. The exfoliation yield of monolayers was measured to be as high as 21% for MoS_2 and 18% for WS_2 in ethanol. Even in pure water, a monolayer yield of 6% for MoS_2 and 5% for WS_2 can be achieved. By reducing the lateral size of the layered crystals to the nanoscale, the edge concentration is drastically increased and can provide sufficient hydrodynamic force to overcome the interlayer van der Waals attraction to delaminate the layered crystals in solution, providing a new strategy for the large-scale production of TMDC monolayers by liquid exfoliation. In addition to demonstrating successful exfoliation, the exfoliated MoS_2 and WS_2 monolayers also exhibit excellent catalytic hydrogen activities, particularly for monolayer WS_2, which has a cocatalytic performance that is even higher than that of Pt.

EXPERIMENTAL SECTION

Synthesis of Bulk MoS_2 and WS_2 Precursors. Bulk MoS_2 and WS_2 precursors were synthesized by thermal decomposition of $(NH_4)_2MoS_4$ (purity 99.5%, Wako) and $(NH_4)_2WS_4$ (purity 99.97, Aldrich) in an Ar atmosphere. The temperature was raised to 800 °C at the rate of 5 °C per minute and maintained for 5 h, then the material was cooled to room temperature naturally.

Exfoliation. Typically, 100 mg of the as-prepared bulk MoS_2 (WS_2) precursor was added into a 100 mL glass vial. Then, 50 mL of polar micromolecular solvent was added as the exfoliation and dispersion solvent. The mixture was bath sonicated for 48 h using an FU-260-C at a frequency of 28 kHz. The resulting suspensions were first centrifuged using a TOMY LC-200 centrifuge at 2000 rpm (RCF 760*g*) for 1 h, then the top 2/3 portions of the supernatants were carefully collected by pipet. The obtained supernatants were added into a new glass vial and sonicated again for another 4 h. Then, the monolayer MoS_2 (WS_2) dispersions were collected by pipet, followed by another centrifugation of the supernatant at 4000 rpm (RCF 3020*g*) for 1 h.

Characterization. The bulk material structures were determined using an X-ray diffractometer (X'pert powder, PANalytical B.V., Netherlands) with Cu Kα radiation. SEM was performed on a JEOL 6701F field-emission scanning electron microscope. TEM was performed on an FEI Tecnai G2 F30 microscope with a 300 kV accelerating voltage. AFM was carried out in tapping mode (Nanocute H, Japan). XPS data were collected using a PHI Quantera SXM (ULVAC-PHI, Japan). Raman spectroscopy was performed using a Horiba Jobin Yvon LabRAM system with a 532 nm excitation laser. UV−vis absorption spectra were measured using a Shimadzu UV-2500 spectrophotometer in quartz cuvettes with a path length of 2 mm. The ζ potential was tested using a zeta-potential and particle size analyzer ELSZ-2000 series.

Preparation of MoS_2/CdS and WS_2/CdS Composites. Monolayer MoS_2 (WS_2) suspensions were mixed with commercial CdS (99%, Aldrich) in different stoichiometric ratios, sonicated, and stirred overnight until dry, and then the composites were collected and annealed in an Ar atmosphere at 400 °C for 4 h.

Photocatalytic Hydrogen Evolution. The photocatalytic H_2 evolution was carried out with 0.2 g of the photocatalyst hybrid in 300 mL of solution in a Pyrex glass reaction cell. The optimized reaction solution is 30 vol % lactic acid adjusted by NaOH to achieve a pH ≈ 5.0. The reaction cell was connected to a closed gas system with a gas circulation pump. A 300 W xenon lamp equipped with L42 cutoff filter was used as the visible light source (λ > 420 nm). H_2 evolution was measured with an online gas chromatograph (GC-8A, Shimadzu) equipped with a thermal conductivity detector according to the standard curve. The AQEs with various monochromatic lights were obtained by using a series of band-pass filters (Optical Coatings Japan). The light intensity was measured using a radiant power energy meter (Ushio spectroradiometer, USR-40, Japan). The AQE was calculated using the following equation:

$$\mathrm{AQE} = \frac{\text{number of reacted electrons}}{\text{number of incident photos}} = \frac{\text{number of evolved } H_2 \text{ molecules} \times 2}{\text{number of incident photos}} = \frac{MN_A 2}{\frac{IAt}{E_g J}}$$

where M represents the amount of H_2 generation, N_A represents Avogadro's constant, I is the light intensity, A is the light incident area, t is the light incident time, and E_g and J are fixed constants.

ASSOCIATED CONTENT

Supporting Information

The Supporting Information is available free of charge on the ACS Publications website at DOI: 10.1021/jacs.6b08096.

TEM data, AFM data, UV−vis spectroscopic data, and photocatalytic H_2 evolution activities (PDF)

AUTHOR INFORMATION

Corresponding Authors

*Chang.Kun@nims.go.jp

*Jinhua.Ye@nims.go.jp

Author Contributions

⊥X.H. and K.C. contributed equal to this work.

Notes

The authors declare no competing financial interest.

ACKNOWLEDGMENTS

The authors acknowledge financial support from the World Premier International Research Center Initiative (WPI Initiative) on Materials Nanoarchitectonics (MANA), MEXT (Japan), National Basic Research Program of China (973 Program, 2014CB239301), Mitsubishi Foundation, the JSPS KAKENHI (Grant No. 16F16049), and the National Science Foundation of China for Young (No. 21303042).

REFERENCES

(1) Novoselov, K. S.; Geim, A. K.; Morozov, S. V.; Jiang, D.; Zhang, Y.; Dubonos, S. V.; Grigorieva, I. V.; Firsov, A. A. *Science* **2004**, *306*, 666−669.

(2) Fan, X. B.; Xu, P. T.; Li, Y. G.; Zhou, D. K.; Sun, Y. F.; Nguyen, M. A. T.; Terrones, M.; Mallouk, T. E. *J. Am. Chem. Soc.* **2016**, *138*, 5143−5149.

(3) Novoselov, K. S.; Jiang, D.; Schedin, F.; Booth, T. J.; Khotkevich, V. V.; Morozov, S. V.; Geim, A. *Proc. Natl. Acad. Sci. U. S. A.* **2005**, *102*, 10451−10453.

(4) Zeng, H.; Dai, J.; Yao, W.; Xiao, D.; Cui, X. *Nat. Nanotechnol.* **2012**, *7*, 490−493.

(5) Wang, Q. H.; Kalantar-Zadeh, K.; Kis, A.; Coleman, J. N.; Strano, M. S. *Nat. Nanotechnol.* **2012**, *7*, 699−712.

(6) Radisavljevic, B.; Radenovic, A.; Brivio, J.; Giacometti, V.; Kis, A. *Nat. Nanotechnol.* **2011**, *6*, 147−150.

(7) Li, T.; Galli, G. *J. Phys. Chem. C* **2007**, *111*, 16192−16196.

DOI: 10.1021/jacs.6b08096
J. Am. Chem. Soc. 2016, 138, 14962−14969

(8) Splendiani, A.; Sun, L.; Zhang, Y. B.; Li, T. S.; Kim, J.; Chim, C. Y.; Galli, G.; Wang, F. *Nano Lett.* **2010**, *10*, 1271−1275.
(9) Lopez-Sanchez, O.; Lembke, D.; Kayci, M.; Radenovic, A.; Kis, A. *Nat. Nanotechnol.* **2013**, *8*, 497−501.
(10) Lee, C.-H.; Lee, G.-H.; van der Zande, A. M.; Chen, W.; Li, Y.; Han, M.; Cui, X.; Arefe, G.; Nuckolls, C.; Heinz, T. F.; Guo, J.; Hone, J.; Kim, P. *Nat. Nanotechnol.* **2014**, *9*, 676−681.
(11) Chang, K.; Li, M.; Wang, T.; Ouyang, S. X.; Li, P.; Liu, L. Q.; Ye, J. H. *Adv. Energy. Mater.* **2015**, *5*, 1402279.
(12) Huang, X.; Zeng, Z. Y.; Zhang, H. *Chem. Soc. Rev.* **2013**, *42*, 1934−1946.
(13) Zhang, H. *ACS Nano* **2015**, *9*, 9451−9469.
(14) Jaramillo, T. F.; Jørgensen, K. P.; Bonde, J.; Nielsen, J. H.; Horch, S.; Chorkendorff, I. *Science* **2007**, *317*, 100−102.
(15) Kibsgaard, J.; Chen, Z. B.; Reinecke, B. N.; Jaramillo, T. F. *Nat. Mater.* **2012**, *11*, 963−969.
(16) Hinnemann, B.; Moses, P. G.; Bonde, J.; Jørgensen, K. P.; Nielsen, J. H.; Horch, S.; Chorkendorff, I.; Nørskov, J. K. *J. Am. Chem. Soc.* **2005**, *127*, 5308−5309.
(17) Chang, K.; Hai, X.; Ye, J. *Adv. Energy Mater.* **2016**, *6*, 1502555−1502575.
(18) Li, H.; Tsai, C.; Koh, A. L.; Cai, L. L.; Contryman, A. W.; Fragapane, A. H.; Zhao, J. H.; Han, H. S.; Manoharan, H. C.; Abild-Pedersen, F.; Nørskov, J. K.; Zheng, X. L. *Nat. Mater.* **2016**, *15*, 48−53.
(19) Nicolosi, V.; Chhowalla, M.; Kanatzidis, M. G.; Strano, M. S.; Coleman, J. N. *Science* **2013**, *340*, 1226419.
(20) Coleman, J. N.; Lotya, M.; O'Neill, A.; Bergin, S. D.; King, P. J.; Khan, U.; Young, K.; Gaucher, A.; De, S.; Smith, R. J.; Shvets, I. V.; Arora, S. K.; Stanton, G.; Kim, H. Y.; Lee, K.; Kim, G. T.; Duesberg, G. S.; Hallam, T.; Boland, J. J.; Wang, J. J.; Donegan, J. F.; Grunlan, J. C.; Moriarty, G.; Shmeliov, A.; Nicholls, R. J.; Perkins, J. M.; Grieveson, E. M.; Theuwissen, K.; McComb, D. W.; Nellist, P. D.; Nicolosi, V. *Science* **2011**, *331*, 568.
(21) Backes, C.; Szydlowska, B. M.; Harvey, A.; Yuan, S.; Vega-Mayoral, V.; Davies, B. R.; Zhao, P.-l.; Hanlon, D.; Santos, E. J. G.; Katsnelson, M. I.; Blau, W. J.; Gadermaier, C.; Coleman, J. N. *ACS Nano* **2016**, *10*, 1589−1601.
(22) Smith, R. J.; King, P. J.; Lotya, M.; Wirtz, C.; Khan, U.; De, S.; O'Neill, A.; Duesberg, G. S.; Grunlan, J. C.; Moriarty, G.; Chen, J.; Wang, J.; Minett, A. I.; Nicolosi, V.; Coleman, J. N. *Adv. Mater.* **2011**, *23*, 3944−3948.
(23) Shen, J.; He, Y.; Wu, J.; Gao, C.; Keyshar, K.; Zhang, X.; Yang, Y.; Ye, M.; Vajtai, R.; Lou, J.; Ajayan, P. M. *Nano Lett.* **2015**, *15*, 5449−5454.
(24) Kim, J.; Kwon, S.; Cho, D.-H.; Kang, B.; Kwon, H.; Kim, Y.; Park, S. O.; Jung, G. Y.; Shin, E.; Kim, W.-G.; Lee, H.; Ryu, G. H.; Choi, M.; Kim, T. H.; Oh, J.; Park, S.; Kwak, S. K.; Yoon, S. W.; Byun, D.; Lee, Z.; Lee, C. *Nat. Commun.* **2015**, *6*, 8294−8302.
(25) Liang, K. S.; Chianelli, R. R.; Chien, F. Z.; Moss, S. C. *J. Non-Cryst. Solids* **1986**, *79*, 251−273.
(26) Chhowalla, M.; Amaratunga, G. A. J. *Nature* **2000**, *407*, 164−167.
(27) Oakes, L.; Carter, R.; Hanken, T.; Cohn, A. P.; Share, K.; Schmidt, B.; Pint, C. L. *Nat. Commun.* **2016**, *7*, 11796.
(28) Lee, C.; Yan, H.; Brus, L. E.; Heinz, T. F.; Hone, J.; Ryu, S. *ACS Nano* **2010**, *4*, 2695−2700.
(29) Halim, U.; Zheng, C. R.; Chen, Y.; Lin, Z.; Jiang, S.; Cheng, R.; Huang, Y.; Duan, X. *Nat. Commun.* **2013**, *4*, 2213.
(30) Wilcoxon, J. P.; Newcomer, P. P.; Samara, G. A. *J. Appl. Phys.* **1997**, *81*, 7934−7944.
(31) Guan, G.; Zhang, S.; Liu, S.; Cai, Y.; Low, M.; Teng, C. P.; Phang, I. Y.; Cheng, Y.; Duei, K. L.; Srinivasan, B. M.; Zheng, Y.; Zhang, Y. W.; Han, M. Y. *J. Am. Chem. Soc.* **2015**, *137*, 6152−6155.
(32) Mak, K. F.; Lee, C.; Hone, J.; Shan, J.; Heinz, T. F. *Phys. Rev. Lett.* **2010**, *105*, 136805.
(33) Backes, C.; Smith, R. J.; McEvoy, N.; Berner, N. C.; McCloskey, D.; Nerl, H. C.; O'Neill, A.; King, P. J.; Higgins, T.; Hanlon, D.; Scheuschner, N.; Maultzsch, J.; Houben, L.; Duesberg, G. S.; Donegan, J. F.; Nicolosi, V.; Coleman, J. N. *Nat. Commun.* **2014**, *5*, 4576.
(34) Li, H.; Zhang, Q.; Yap, C. C. R.; Tay, B. K.; Edwin, T. H. T.; Olivier, A.; Baillargeat, D. *Adv. Funct. Mater.* **2012**, *22*, 1385−1390.
(35) Chou, S. S.; De, M.; Kim, J.; Byun, S.; Dykstra, C.; Yu, J.; Huang, J.; Dravid, V. P. J. *J. Am. Chem. Soc.* **2013**, *135*, 4584−4587.
(36) Wang, L.; Xu, Z.; Wang, W.; Bai, X. *J. Am. Chem. Soc.* **2014**, *136*, 6693−6697.
(37) Oakes, L.; Zulkifli, D.; Azmi, H.; Share, K.; Hanken, T.; Carter, R.; Pint, C. L. *J. Electrochem. Soc.* **2015**, *162*, D3063−D3070.
(38) Voiry, D.; Salehi, M.; Silva, R.; Fujita, T.; Chen, M.; Asefa, T.; Shenoy, V. B.; Eda, G.; Chhowalla, M. *Nano Lett.* **2013**, *13*, 6222−6227.
(39) Hunter, R. J. *Zeta potential in colloid science: Principles and applications*; Academic Press: London, 1981.
(40) Zou, X. X.; Zhang, Y. *Chem. Soc. Rev.* **2015**, *44*, 5148−5180.
(41) Chen, J.; Wu, X.-J.; Yin, L.; Li, B.; Hong, X.; Fan, Z.; Chen, B.; Xue, C.; Zhang, H. *Angew. Chem., Int. Ed.* **2015**, *54*, 1210−1214.
(42) Cheng, L.; Huang, W. J.; Gong, Q. G.; Liu, C. H.; Liu, Z.; Li, Y. G.; Dai, H. J. *Angew. Chem., Int. Ed.* **2014**, *53*, 7860−7863.
(43) Tong, H.; Ouyang, S. X.; Bi, Y. P.; Umezawa, N.; Oshikiri, M.; Ye, J. H. *Adv. Mater.* **2012**, *24*, 229−251.
(44) Yan, H.; Yang, J.; Ma, G.; Wu, G.; Zong, X.; Lei, Z.; Shi, J.; Li, C. *J. Catal.* **2009**, *266*, 165−168.
(45) Mcateer, D.; Gholamvand, Z.; Mcevoy, N.; Harvey, A.; O'Malley, E.; Duesberg, G. S.; Coleman, J. N. *ACS Nano* **2016**, *10*, 672−683.
(46) Huang, Q.; Tian, S.; Zeng, D.; Wang, X.; Song, W.; Li, Y.; Xiao, W.; Xie, C. *ACS Catal.* **2013**, *3*, 1477−1485.
(47) Woan, K.; Pyrgiotakis, G.; Sigmund, W. *Adv. Mater.* **2009**, *21*, 2233−2239.
(48) Zhang, H.; Lv, X.; Li, Y.; Wang, Y.; Li, J. *ACS Nano* **2010**, *4*, 380−386.

DOI: 10.1021/jacs.6b08096
J. Am. Chem. Soc. 2016, 138, 14962−14969